15

Advanced Numerical Techniques for Near-Field Antenna Measurements

Sandra Costanzo and Giuseppe Di Massa
University of Calabria
Italy

1. Introduction

The evaluation of antenna radiation features requires the accurate determination of its far-field pattern, whose direct measurement imposes to probe the field at a distance proportionally related to the ratio between the squared dimension *D* of the antenna aperture and the excitation wavelength (Fig.1). As a consequence of this, the direct evaluation of antenna far-field pattern could require prohibitive distances in the presence of electrically large radiating systems, with increasing complexity and cost of the measurement setup in order to minimize interfering effects.

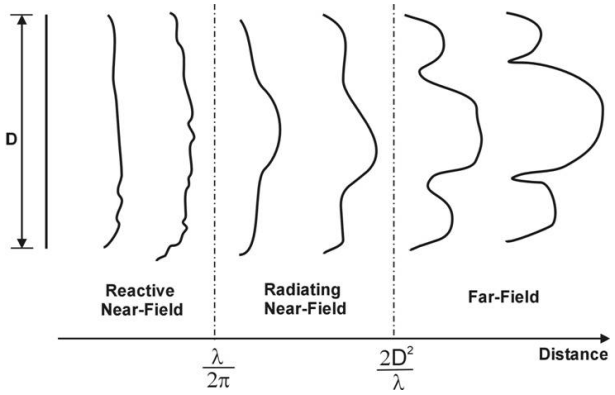

Fig. 1. Antenna field regions.

To face the problem of impractical far-field ranges, the idea to recover far-field patterns from near-field measurements (Johnson et al., 1973) has been introduced and is largely adopted today, as leading to use noise controlled test chambers with reduced size and costs. The near-field approach relies on the acquisition of the tangential field components on a prescribed scanning surface, with the subsequent far-field evaluation essentially based on a modal expansion inherent to the particular geometry (Yaghajian, 1986). The accuracy and performances of near-field methods are strictly limited by the effectiveness of the related transformation algorithms as well as by the measurement accuracy of available input data, and in particular of near-field phase, which is very difficult to obtain at high operating frequencies. In relation to the above aspects, two classes of methods are discussed in this chapter, the first one concerning efficient transformation algorithms for not canonical

near-field surfaces, and the second one relative to accurate far-field characterization by near-field amplitude-only (or phaseless) measurements.

2. Efficient near-field to far-field transformations on strategic scanning surfaces

Near-field to far-field (NF-FF) transformation algorithms, taking also into account for the presence of non-ideal probes, have been developed in literature for the most common scanning surfaces of planar, cylindrical and spherical type (Yaghajian, 1986). All these canonical near-field geometries have their own features, limiting in some way the applicability of the related near-field technique. Due to its intrinsic simplicity, from both the analytical and the computational viewpoints, the planar (Fig. 2(a)) near-field configuration (Wang, 1988) results to be the most attractive one, suffering however of a limited spatial resolution which allows an efficient application only in the presence of highly directive antennas with pencil beam patterns. Slightly greater computational efforts are required by the near-field cylindrical (Fig. 2(b)) scanning (Leach and Paris, 1973), leading to obtain a complete far-field azimuth pattern, with the only exclusion of elevation angles equal to 0 and 180 degrees, for which the Hankel function is not defined (Johnson et al., 1973). A full pattern reconstruction is assured by the near-field spherical (Fig. 2(c)) scanning (Ludwig, 1971), which however requires a complicated measurement setup and a time consuming transformation algorithm for the computation of the relative expansion coefficients.

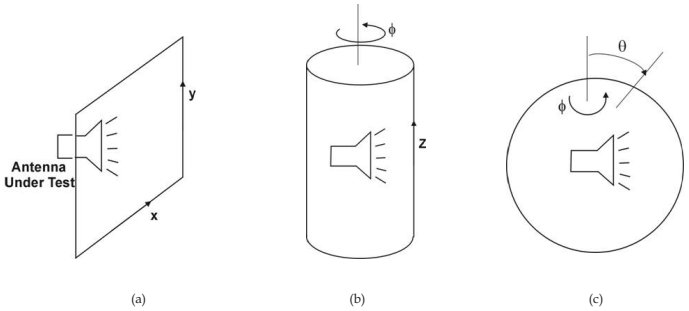

Fig. 2. Canonical near-field scannings: (a) planar, (b) cylindrical, (c) spherical.

In order to reduce the acquisition time as well as to enlarge the scan area, innovative configurations have been proposed in recent years as variant to the most common planar and cylindrical scannings. These new acquisition geometries, namely the helicoidal (Costanzo and Di Massa, 2004), plane-polar (Costanzo and Di Massa, 2006 a), bi-polar (Costanzo and Di Massa, 2006 b) and spiral ones (Costanzo and Di Massa, 2007), give a simpler, more compact and less expensive scanning setup, by imposing a continuous motion of the antenna under test (AUT) and the measuring probe. However, due to the non-standard location of the near-field data points, these innovative configurations strongly complicate, in principle, the NF-FF transformation process, as a conversion to a rectangular data format, in the case of plane-polar, bi-polar and spiral geometries, or to a cylindrical format, in the case of helicoidal scanning, is generally required to enable the application of standard NF-FF planar or cylindrical transformations. In some recent papers (Costanzo and Di Massa, 2004; 2006 a;b; 2007), direct NF-FF algorithms have been proposed to obtain the far-field pattern from near-field data acquired on the above strategic geometries, by properly apply the fast Fourier transform (FFT) and the related shift property (Bracewell, 2000) to avoid any kind of intermediate interpolation. The theoretical details of the above efficient NF-FF transformation procedures are discussed in the next sections.

2.1 Helicoidal NF-FF transformation

In the helicoidal scanning configuration (Fig. 3), near-field data are acquired on a cylindrical helix of radius r_o at sample points $P_e\,(r_o, \phi_o, z_o)$, by imposing a simultaneous linear movement (along z-axis) of the probe and an azimuthal rotation of the AUT (Costanzo and Di Massa, 2004).

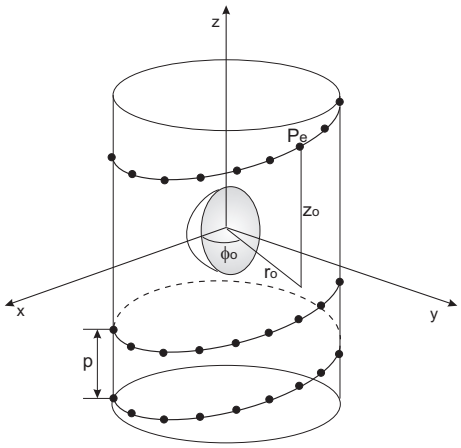

Fig. 3. Helicoidal near-field scanning.

The tangential field components on the helicoidal surface can be expressed in terms a cylindrical modal expansion (Leach and Paris, 1973), with coefficients a_n, b_n given by the expressions:

$$b_n(h)\frac{\Lambda^2}{k}H_n^{(2)}\,(\Lambda r_o) = \frac{1}{4\pi^2}\int_{-\infty}^{+\infty}\int_{-\pi}^{+\pi} E_z(\phi_o, z_o)e^{-jn\phi_o}e^{jhz_o}d\phi_o dz_o \tag{1}$$

$$b_n(h)\frac{nh}{kr_o}H_n^{(2)}\,(\Lambda r_o) - a_n(h)\frac{\partial H_n^{(2)}}{\partial r}(\Lambda r)|_{r=r_o} = \frac{1}{4\pi^2}\int_{-\infty}^{+\infty}\int_{-\pi}^{+\pi} E_\phi(\phi_o, z_o)e^{-jn\phi_o}e^{jhz_o}d\phi_o dz_o \tag{2}$$

where k is the free-space propagation factor, $\Lambda = \sqrt{k^2 - h^2}$ and $H_n^{(2)}(..)$ is the Hankel function of the second kind and order n (Abramowitz and Stegun, 1972).
In the standard case of a near-field acquisition on a cylinder of radius r_o, integrals appearing into equations (1) and (2) are efficiently evaluated by a two-dimensional FFT, by assuming sampling spacings $\Delta\phi = \frac{\lambda}{2a}$ and $\Delta z = \frac{\lambda}{2}$, a being the radius of the smallest cylinder completely enclosing the AUT. The far-field is finally obtained in terms of asymptotic evaluation of cylindrical wave expansion (Leach and Paris, 1973) as:

$$E_\theta(\theta, \phi) = jsin\theta \sum_{n=-\infty}^{+\infty} j^n b_n(kcos\theta)e^{jn\phi} \tag{3}$$

$$E_\phi(\theta, \phi) = sin\theta \sum_{n=-\infty}^{+\infty} j^n a_n(kcos\theta)e^{jn\phi} \tag{4}$$

In the case of helicoidal near-field acquisition as illustrated in Fig. 3, the azimuthal and z-axis coordinates are related by the equation:

$$z_o = p\frac{\phi_o}{2\pi} \tag{5}$$

where p is the helix step, i.e. the distance between adjacent points along a generatrix. By imposing $p = \frac{\lambda}{2}$, near-field data on the cylindrical helix can be arranged into a matrix $\underline{\underline{A}} \in \mathcal{C}^{MxN}$, M being the number of helicoidal revolutions and N the number of azimuthal samples for each revolution. Data distributed on the $i-th$ column of matrix $\underline{\underline{A}}$ are shifted with respect to the first column by a quantity $i\Delta z_\phi$, where $\Delta z_\phi = p\frac{\Delta\phi}{2\pi}$. This particular data arrangement leads to efficiently solve integrals involved in the computation of modal expansions coefficients $a_n(h)$,$b_n(h)$ as given by equations (1) and (2). If we consider the numerical implementation of integral:

$$I_n(h) = \frac{1}{4\pi^2}\int_{-\infty}^{+\infty}\int_{-\infty}^{+\infty} E_z\left(\phi_o, z_o\right) e^{-jn\phi_o} e^{jhz_o} d\phi_o dz_o \tag{6}$$

which appears into equation (1), after some manipulations (Costanzo and Di Massa, 2004) we can write:

$$I_n(h) = \sum_{r=0}^{N-1} \widetilde{E}_{zs}\left(r\Delta\phi, h\right) e^{-j\frac{2\pi nr}{N}} \tag{7}$$

where the term:

$$\widetilde{E}_{zs}\left(r\Delta\phi, h\right) = \widetilde{E}_z\left(r\Delta\phi, h\right) e^{-j\frac{2\pi hr\Delta z_\phi}{M}} \tag{8}$$

represents the discrete Fourier transform (DFT) (Bracewell, 2000) of the sequence $E_z\left(r\Delta\phi, s\Delta z\right)$, axially translated by a quantity $r\Delta z_\phi$ through the application of the Fourier transform shift property (Bracewell, 2000).
The computation procedure for integral (6), described by equation (7), can be summarized by the following steps:

1. given the tangential component E_z on the helicoidal surface, perform FFT on each column of matrix data $\underline{\underline{A}}$;
2. apply the Fourier transform shift property to the transformed columns obtained from step 1;
3. perform FFT on the rows to obtain the final result in (7);

The outlined procedure can be obviously repeated for the computation of integral appearing into equation (2), which involves the component E_ϕ. Combined results are finally used to determine the expansion coefficients $a_n(h)$, $b_n(h)$, giving the far-field pattern components (3), (4).
The far-field reconstruction process from helicoidal near-field data is validated by performing numerical simulations on a linear array of z-oriented 37 elementary Huyghens sources, $\lambda/2$ spaced along z-axis (Costanzo and Di Massa, 2004). Near-field samples are collected on a cylindrical helix of radius $r_o = 21.5\lambda$ and height equal to 120λ, with an azimuthal sampling step $\Delta\phi = 2.38^o$. The effectiveness of the helicoidal NF-FF transformation procedure is demonstrated under Fig. 4, where the computed far-field pattern for the dominant E_θ component is successfully compared with that obtained from a standard cylindrical NF-FF transformation on a cylindrical surface having the same radius and height as those relative to the helicoidal acquisition curve.

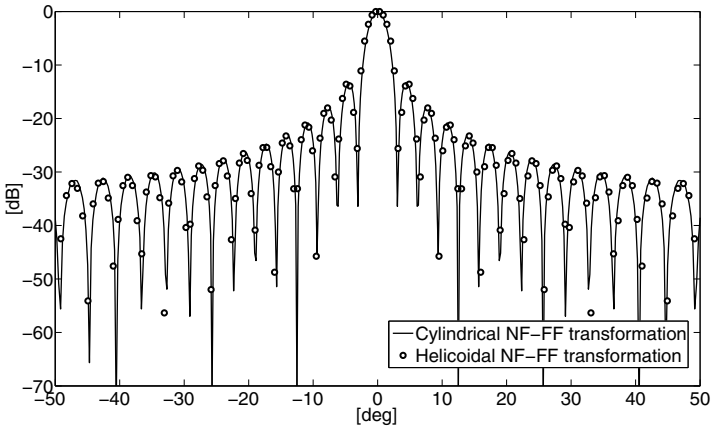

Fig. 4. Far-field amplitude (E_θ component) for linear array of z-oriented 37 elementary Huyghens sources: comparison between cylindrical and helicoidal NF-FF transformations.

2.2 NF-FF transformations on innovative planar-type geometries

The coordinate system relevant to the acquisition scheme for the planar-type geometries is illustrated in Fig. 5, where the measuring probe moves on the $z = 0$ plane to collect the near-field coming from a test antenna mounted on the z-axis.

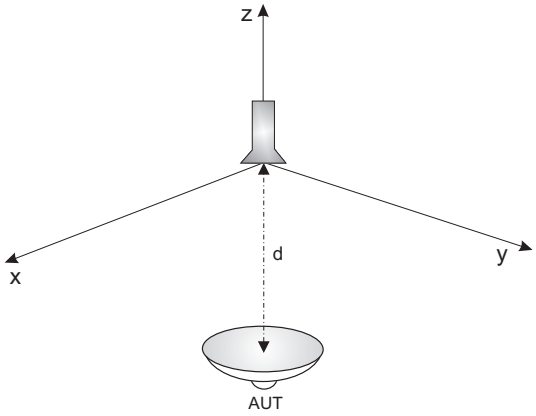

Fig. 5. Coordinate system relevant to the near-field planar-type acquisition scheme.

The mathematical relationship between the antenna field and the probe equivalent aperture currents can be easily found by applying Lorentz reciprocity (Costanzo and Di Massa, 2006 a) to have:

$$T(\theta,\phi) = \int_{-\infty}^{+\infty}\int_{-\infty}^{+\infty} q(x',y')e^{jk(x'sin\theta cos\phi + y'sin\theta sin\phi)}dx'dy' \tag{9}$$

Under the simplified assumption of an infinitesimal ideal probe, the left hand side of equation (9) expressed in its scalar form, gives the antenna radiation pattern at coordinates (θ,ϕ), while the term $q(x',y')$ represents the near-field probed at coordinates (x',y').

If we consider a near-field polar surface of radius a, the following expression (Costanzo and Di Massa, 2006 a) can be derived for the radiation integral:

$$T(\theta,\phi) = \int_0^a \int_0^{2\pi} q(\rho',\phi') e^{jk\rho' sin\theta cos(\phi-\phi')} \rho' d\rho' d\phi' \tag{10}$$

where the coordinates transformations $x' = \rho' cos\phi'$ and $y' = \rho' sin\phi'$ are applied.
The inner integral into relation (10) can be easily recognized as a convolution with respect to the azimuthal variable ϕ', so the convolution theorem (Bracewell, 2000) can be applied to simplify its computation in terms of FFT. By exploiting this convolution property, compact expressions of equation (10) can be derived for the plane-polar, bi-polar and planar spiral configurations, as it will be discussed in the follows.

2.2.1 NF-FF transformation on plane-polar geometry

In the plane-polar configuration (Fig. 6), near-field data are acquired on concentric rings filling a disk of radius a, with sampling steps in the radial and azimuthal directions given by the expressions:

$$\Delta\rho = \frac{\lambda}{2}, \qquad \Delta\phi = \frac{\lambda}{2r_o} \tag{11}$$

r_o being the radius of the smallest sphere enclosing the AUT.

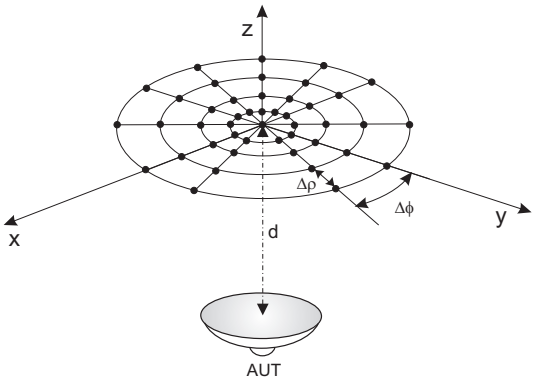

Fig. 6. Plane-polar near-field scanning.

In the presence of polar near-field samples, equation (10) can be expressed in a compact form as (Costanzo and Di Massa, 2006 a):

$$T(\theta,\phi) = \int_0^a \int_0^{2\pi} q_1(\rho',\phi') r(\theta,\phi,\rho',\phi') d\rho' d\phi' \tag{12}$$

where:

$$q_1(\rho',\phi') = \rho' q(\rho',\phi'), \qquad r(\theta,\phi,\rho',\phi') = e^{jk\rho' sin\theta cos(\phi-\phi')} \tag{13}$$

The convolution form with respect to the azimuthal variable ϕ' leads to express (13) in terms of FFT as:

$$T(\theta,\phi) = \int_0^a \mathcal{F}^{-1} \left\{ \widetilde{q}_1(\rho', w) \widetilde{r}(\theta,\phi,\rho', w) \right\} d\rho' \tag{14}$$

where the symbol $\mathcal{F}\{..\}$ and the tilde $(\tilde{})$ on the top denote the Fourier transform operator. If we consider a plane-polar near-field data set at coordinates $(m\Delta\rho, n\Delta\phi)$, with $m = 0, ...M-1$, $n = 0, ..., N-1$, M being the number of concentric rings and N the number of sectors, the radiation integral (14) can be numerically implemented as:

$$T(\theta,\phi) = \sum_{m=0}^{M-1}\sum_{n=0}^{N-1}\left[\tilde{q}_1\left(m\Delta\rho, w\right)\tilde{r}\left(\theta,\phi,m\Delta\rho,w\right)\right]e^{j\frac{2\pi n' w}{N}} \tag{15}$$

where the terms: $\tilde{q}_1\left(m\Delta\rho, w\right)$ and $\tilde{r}\left(\theta,\phi,m\Delta\rho,w\right)$ represent the DFT of the sequences $q_1(..)$ and $r(..)$ with respect to the azimuthal coordinate ϕ'.
The computation scheme given by equation (15) can be summarized by the following steps:

1. multiply the near-field plane-polar samples by the radial coordinate ρ';
2. perform FFT on the result coming from step 1 with respect to the azimuthal coordinate ϕ';
3. perform FFT on the exponential function $e^{jk\rho' sin\theta cos(\phi-\phi')}$ with respect to the azimuthal coordinate ϕ'
4. compute the inverse FFT on the product of results coming from steps 2 and 3;
5. perform summation on the result coming from step 4 with respect to the radial coordinate ρ'.

2.2.2 NF-FF transformation on bi-polar geometry

In the bi-polar geometry, the positions of the near-field samples lying on radial arcs can be completely described in terms of the probe arm length L and the angles α, β, giving the rotations of the AUT and the probe, respectively (Fig. 7).

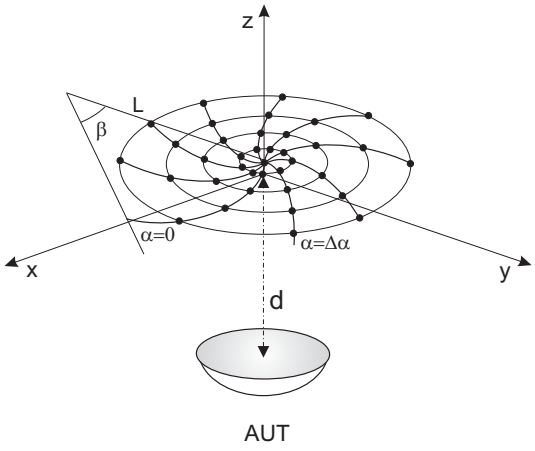

Fig. 7. Bi-polar near-field scanning.

As a consequence of this, a curvilinear coordinate system can be used to describe the scanning grid and the radiation integral (10) can be expressed as (Costanzo and Di Massa, 2006 b):

$$T(\theta,\phi) = L^2\int_0^{\beta_{max}}\int_{\frac{\beta'}{2}}^{\frac{\beta'}{2}+2\pi} q\left(\alpha',\beta'\right)e^{j2kLsin\theta sin\left(\frac{\beta'}{2}\right)cos\left(\phi-\alpha'+\frac{\beta'}{2}\right)}sin\beta' d\beta' d\alpha' \tag{16}$$

where β_{max} is the maximum angular extent and the following transformations from polar coordinates (ρ, ϕ) to curvilinear coordinates (α, β) are applied:

$$\rho = 2Lsin\left(\frac{\beta}{2}\right), \qquad \phi = \alpha - \frac{\beta}{2} \tag{17}$$

The inner integral into relation (16) can be easily recognized as a convolution in the variable α', so the convolution theorem can be invoked to obtain the equivalent form:

$$T(\theta, \phi) = \int_0^{\beta_{max}} \mathcal{F}^{-1}\left\{\widetilde{q}_1(w, \beta')\widetilde{r}(\theta, \phi, w, \beta')\right\} d\beta' \tag{18}$$

where:

$$q_1(\alpha', \beta') = L^2 q(\alpha', \beta') sin\beta', \qquad r(\theta, \phi, \alpha', \beta') = e^{j2kLsin\theta sin\left(\frac{\beta'}{2}\right)cos\left[\left(\phi + \frac{\beta'}{2}\right) - \alpha'\right]} \tag{19}$$

Let us consider a bi-polar scanning grid, with near-field samples located at coordinates $(m\Delta\alpha, n\Delta\beta)$, $m = 0, ...M-1$, $n = 0, ..., N-1$, M being the number of arcs and N the number of measurement points along each arc. Incremental steps $\Delta\alpha$, $\Delta\beta$ coherent with the sampling requirements inherent to the plane-polar configurations are assumed, by imposing relations (11) into expressions (17). Under the above assumptions, the numerical implementation of integral (18) is given as (Costanzo and Di Massa, 2006 b):

$$T(\theta, \phi) = \sum_{n=0}^{N-1} \sum_{m=0}^{M-1} \left[\widetilde{q}_1\left(w, n\Delta\beta\right) \widetilde{r}\left(\theta, \phi, w, n\Delta\beta\right)\right] e^{j\frac{2\pi m' w}{M}} \tag{20}$$

where the terms $\widetilde{q}_1\left(w, n\Delta\beta\right)$ and $\widetilde{r}\left(\theta, \phi, w, n\Delta\beta\right)$ represent the DFT of the sequences $q_1(..)$ and $r(..)$ with respect to the azimuthal coordinate α'.
The above computation procedure can be summarized by the following steps:

1. multiply the near-field bi-polar data by the term $L^2 sin\beta'$;
2. perform FFT on the result coming from step 1 with respect to the azimuthal coordinate α';
3. perform FFT on the exponential function $e^{j2kLsin\theta sin\left(\frac{\beta'}{2}\right)cos\left(\phi - \alpha' + \frac{\beta'}{2}\right)}$ with respect to the azimuthal coordinate α';
4. compute the inverse FFT on the product of results coming from steps 2 and 3;
5. perform summation on the result coming from step 4 with respect to the angular coordinate β'.

2.2.3 NF-FF transformation on planar spiral geometry

The planar spiral scanning (Costanzo and Di Massa, 2007) is derived from the bi-polar configuration by imposing the simultaneous rotation of the AUT and the measuring probe in terms of angles α' and β', respectively. This gives a samples arrangement at positions described by the coordinates s' and α' (Fig. 8), where:

$$s' = \frac{\rho'}{d}, \qquad \alpha' = \phi' + \frac{\beta'}{2} \tag{21}$$

d being the distance between the AUT and the measurement plane.
By applying the coordinates transformation (21) into equation (10), the following expression is derived for the radiation integral (Costanzo and Di Massa, 2007):

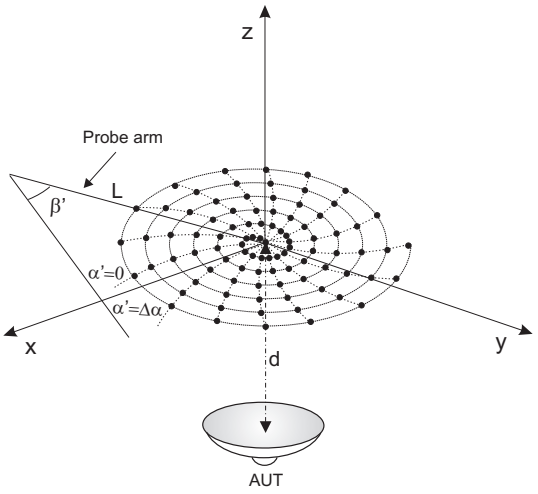

Fig. 8. Planar spiral near-field scanning.

$$T(\theta,\phi)=\int_0^{\frac{\rho max}{d}}\int_{\frac{\beta'}{2}}^{\frac{\beta'}{2}+2\pi} q(s',\alpha')e^{j2kds'sin\theta cos\left(\phi-\alpha'+\frac{\beta'}{2}\right)}d^2s'ds'd\alpha' \tag{22}$$

A compact form of equation (22) can be written as:

$$T(\theta,\phi)=\int_0^{\frac{\rho max}{d}}\int_{\frac{\beta'}{2}}^{\frac{\beta'}{2}+2\pi} q_1(s',\alpha')r(\theta,\phi,s',\alpha')ds'd\alpha' \tag{23}$$

where:

$$q_1(s',\alpha')=d^2s'q(s',\alpha'),\qquad r(\theta,\phi,s',\alpha')=e^{j2kds'sin\theta cos\left[\left(\phi+\frac{\beta'}{2}\right)-\alpha'\right]} \tag{24}$$

Following a similar procedure as that applied to the plane-polar and bi-polar configurations, the convolution form of the inner integral into equation (22) is exploited to obtain the following simplified form in terms of FFT (Costanzo and Di Massa, 2007):

$$T(\theta,\phi)=\int_0^{\frac{\rho max}{d}}\mathcal{F}^{-1}\left\{\widetilde{q}_1(s',w)\widetilde{r}(\theta,\phi,s',w)\right\}ds' \tag{25}$$

Let us assume a spiral trajectory with near-field samples located at coordinates $\alpha_m = m\Delta\alpha$, $s_m = \frac{\rho_{mn}}{d}$, $m = 0,..,M-1$, $n = 0,...,N-1$, where $\rho_{mn} = a(\alpha_m + 2\pi n)$, a being the Archimedean spiral parameter, N the number of loops in the spiral arrangement and M the number of samples for each loop.

The above assumptions on the near-field samples distribution lead to express the numerical computation of radiation integral (25) as:

$$T(\theta,\phi)=\sum_{n=0}^{N-1}\sum_{m=0}^{M-1}\left[\widetilde{q}_1\left(s_{nm},w\right)\widetilde{r}\left(\theta,\phi,s_{nm},w\right)\right]e^{j\frac{2\pi m'w}{M}} \tag{26}$$

where the terms $\widetilde{q}_1\left(s_{nm},w\right)$ and $\widetilde{r}\left(\theta,\phi,s_{nm},w\right)$ denotes the DFT of the sequences $q_1(..)$ and $r(..)$ with respect to the angular variable α'.

A schematic overview of the processing method for far-field computation from near-field samples on planar spiral geometry is reported under Fig. 9.

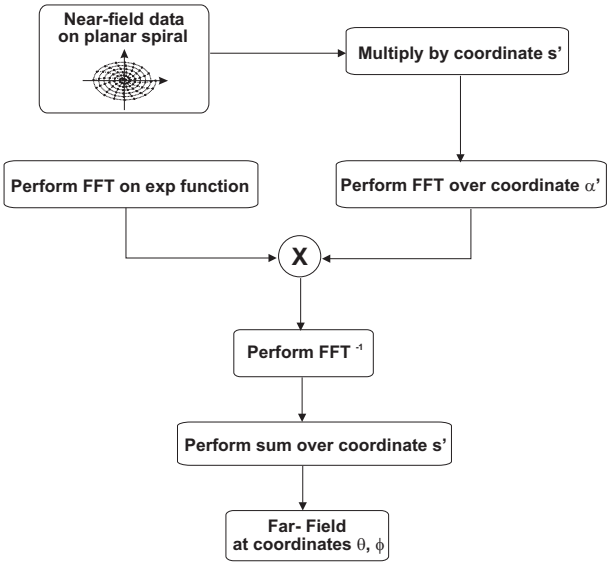

Fig. 9. Flow-chart of NF-FF transformation on planar spiral geometry.

2.2.4 Numerical validations on planar-type NF-FF transformation processes

Numerical simulations are performed on elementary dipole arrays to assess the validity of the NF-FF processing schemes illustrated in the previous paragraphs. As a first example, a near-field bi-polar acquisition is considered on a square array of $21x21$ y-oriented Huyghens sources $\lambda/2$ spaced each others along x and y axes. The array elements are excited with a $20dB$, $n = 2$ Taylor illumination (Elliott, 2003), scanned to an angle $\theta = 15^o$ in the H-plane. A scan plane of radius $a = 10\lambda$, at a distance $d = 6\lambda$ from the AUT, is sampled with angular spacings $\Delta\alpha = 5.2^o$ and $\Delta\beta = 0.38^o$. The normalized amplitude of the simulated near-field is reported under Fig. 10, while the H-plane pattern resulting from the processing scheme is successfully compared in Fig. 11 with the exact radiation pattern coming from the analytical solution.

As a further example, a circular array of 10 y-oriented elementary dipoles $\lambda/2$ spaced is considered, with excitation coefficients chosen to have a main lobe in the direction $\theta = 10^o$ in the H-plane. Simulations are performed on a planar spiral with $N = 20$ loops and $M = 136$ points along each loop, at a distance $d = 10\lambda$ from the AUT. The normalized near-field amplitude is shown in the contour plot of Fig. 12, while the H-plane pattern obtained from the direct transformation algorithm is successfully compared in Fig. 13 with the exact array solution.

3. Hybrid approach for phaseless near-field measurements

The standard near-field approach requires the knowledge of the complex tangential components (both in amplitude and phase) on the prescribed scanning surface. Near-field data are generally collected by a vector receiver and numerically processed to efficiently

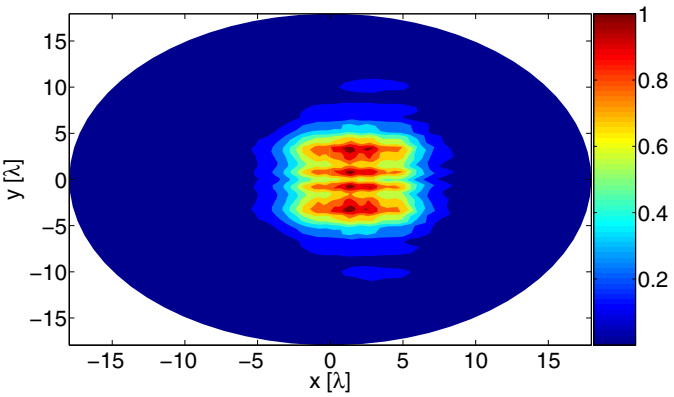

Fig. 10. Normalized bi-polar near-field amplitude for a 21x21 dipole array with Taylor illumination.

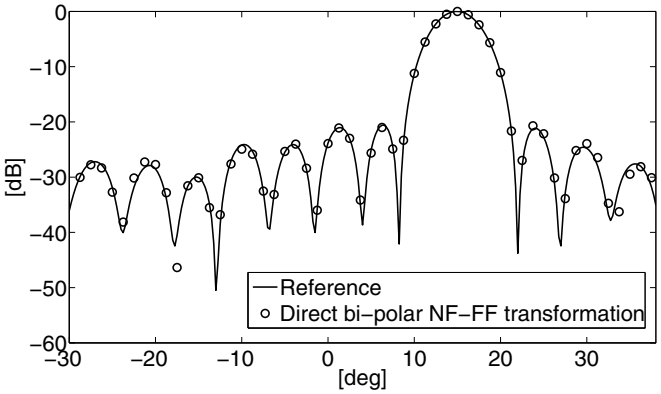

Fig. 11. Co-polarized H-plane pattern for a 21x21 dipole array with Taylor illumination.

evaluate the far-field pattern. The accuracy and performances of NF-FF transformations essentially rely on the precision of the measurement setup and the positioning system, with increasing complexity and cost when dealing with electrically large antennas. As a matter of fact, accurate phase measurements are very difficult to obtain at millimeter and sub-millimeter frequency ranges, unless expensive facilities are used. To overcome this problem, new advanced techniques have been recently developed which evaluate the far-field pattern from the knowledge of the near-field amplitude over one or more testing surfaces (Isernia et al., 1991; 1996). Generally speaking, two classes of phaseless methods can be distinguished, the one based on a functional relationship within a proper set of amplitude-only data (Pierri et al., 1999), the other adopting interferometric techniques (Bennet et al., 1976). In some recent works (Costanzo et al., 2001; Costanzo and Di Massa, 2002; Costanzo et al., 2005; 2008), a novel hybrid procedure has been proposed which combines all the best features of the two kinds of phaseless methods. A basically interferometric approach is adopted, but avoiding the use of a reference antenna as required in standard interferometry. The phase reference is directly obtained from the field radiated by the AUT, which is collected by two probes on two

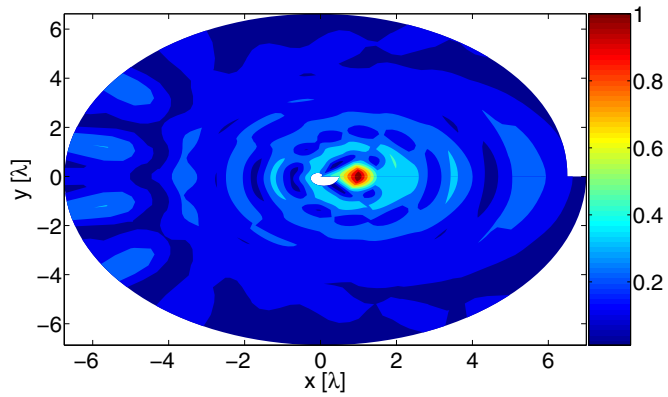

Fig. 12. Normalized bi-polar near-field amplitude for a 21x21 dipole array with Taylor illumination.

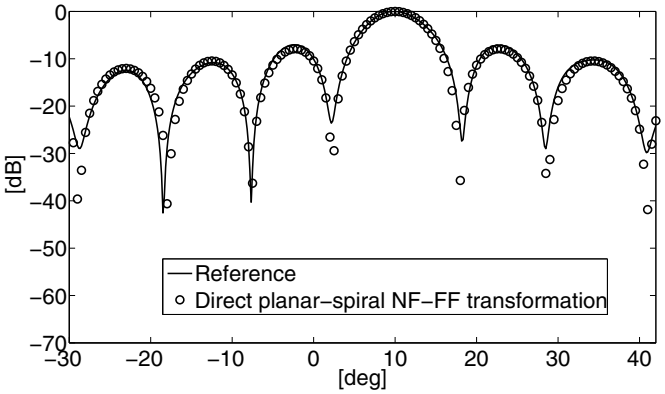

Fig. 13. Co-polarized H-plane pattern for a 21x21 dipole array with Taylor illumination.

different points along the scanning curve to interfere by means of a simple microstrip circuit (Costanzo et al., 2001; Costanzo and Di Massa, 2002). A certain number of sets of retrieved near-field phase results from the application of the proposed interferometric technique. Each set includes phase values on different measurement points, apart from a constant phase shift to be determined. The union of these sets provides the full near-field phase information along the scanning curve, but a complete characterization obviously requires the evaluation of all unknown phase shifts, one for each set. This problem is solved by taking advantages of the analytical properties of the field radiated by the AUT. In particular, a non redundant representation is adopted which is based on the introduction of the reduced field (Bucci et al., 1998), obtained from the original field after extracting a proper phase function and introducing a suitable parameterization along the observation curve. Following this approach, the radiated field on each scanning line is easily identified from the knowledge of the dimension and shape of the AUT. The procedure is repeated along a proper number of observation curves to cover the whole measurement surface. The proposed approach gives a hybrid procedure placed "half the way" between interferometric techniques and functional relationship based

methods. In particular, it takes advantages of the interferometric approach to significantly reduce the number of unknowns in the phase retrieval algorithm. Although the functional to be minimized is highly non-linear, the lower number of unknowns, given by the phase shifts, allows an accurate and fast convergence to the solution. Furthermore, the absence of a reference antenna gives a simpler and more compact measurement setup.

3.1 Theoretical formulation of hybrid phase-retrieval technique

Let us consider an observation curve C over an arbitrary scanning geometry (Fig. 14), with a sampling step $\Delta s = \lambda/2$ and a separation $d = i\lambda/2$ between two adjacent interference points, i being an integer greater than one. Two identical probes simultaneously moving along the measurement curve (Fig. 14) are used to obtain four amplitude information, namely (Costanzo et al., 2001; Costanzo and Di Massa, 2002; Costanzo et al., 2005):

$$|V_1|^2, \quad |V_2|^2, \quad |V_1 + V_2|^2, \quad |V_1 + jV_2|^2 \tag{27}$$

where:

$$V_1 = |V_1| \cdot e^{j\varphi_1}, \quad V_2 = |V_2| \cdot e^{j\varphi_2} \tag{28}$$

are the complex signals on a pair of interference points along C.

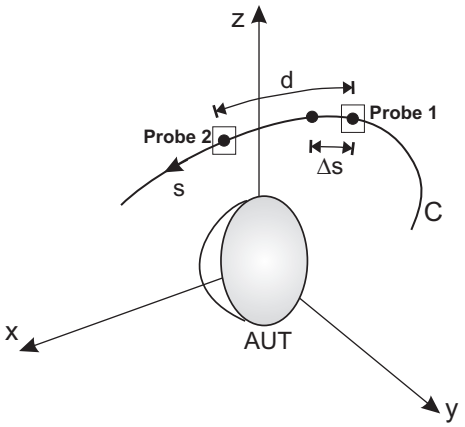

Fig. 14. Observation curve C with probes positions.

Intensity data (27) are processed to give the phase shift $\Delta\varphi = \varphi_1 - \varphi_2$ by means of the following interferometric formula (Costanzo et al., 2001; Costanzo and Di Massa, 2002):

$$\Delta\varphi = tg^{-1}\left[\frac{|V_1 + jV_2|^2 - |V_1|^2 - |V_2|^2}{|V_1 + V_2|^2 - |V_1|^2 - |V_2|^2}\right] \tag{29}$$

Let be:

$$E(s) = |E(s)| \cdot e^{j\varphi(s)} \tag{30}$$

the field radiated by the AUT on the observation curve C, where parameter s denotes the curvilinear abscissa along C (Fig. 14). If we suppose to scan 2N+1 measurement points (N even), the application of equation (29) gives a number of sets of complex near-field data equal to i, namely (Costanzo et al., 2001; 2005):

$$\left[E\left(s_{(1)}\right), E\left(s_{(2)}\right) = \varepsilon\left(s_{(2)}\right) \cdot e^{j\Delta\phi_1}, E\left(s_{(3)}\right) = \varepsilon\left(s_{(3)}\right) \cdot e^{j\Delta\phi_2}, \ldots \right.$$
$$\left. \ldots, E\left(s_{(i)}\right) = \varepsilon\left(s_{(i)}\right) \cdot e^{j\Delta\phi_{i-1}}\right] \tag{31}$$

wherein:

$$\begin{aligned}
s_{(1)} &= \left[-N\frac{\lambda}{2}, (-N+i)\frac{\lambda}{2}, (-N+2i)\frac{\lambda}{2}, \ldots\right] \\
s_{(2)} &= \left[(-N+1)\frac{\lambda}{2}, (-N+i+1)\frac{\lambda}{2}, \right. \\
&\qquad \left. (-N+2i+1)\frac{\lambda}{2}, \ldots\right] \\
&\vdots \\
s_{(i)} &= \left[(-N+i-1)\frac{\lambda}{2}, (-N+2i-1)\frac{\lambda}{2}, \right. \\
&\qquad \left. (-N+3i-1)\frac{\lambda}{2}, \ldots\right]
\end{aligned} \tag{32}$$

The terms $\underline{\varepsilon}\left(s_{(2)}\right), \underline{\varepsilon}\left(s_{(3)}\right), \ldots, \underline{\varepsilon}\left(s_{(i)}\right)$ into expression (31) are known quantities and the phase shifts $\Delta\phi_1, \Delta\phi_2, \ldots, \Delta\phi_{i-1}$ are the unknowns to be determined. If we change $\Delta\phi_1, \Delta\phi_2, \ldots, \Delta\phi_{i-1} \in [-\pi, \pi[$, expression (31) gives the set S_m of all fields compatible with the measured data. The field radiated by the AUT is so given by the intersection $S_m \cap S_A$, where S_A is the set of all fields that the AUT can radiate.

In order to successfully retrieve the unknown phase shifts $\Delta\phi_1, \Delta\phi_2, \ldots, \Delta\phi_{i-1}$, a non redundant representation is adopted which substitutes the original field (30) with the reduced field (Bucci et al., 1998) $F(\xi) = E(\xi) \cdot e^{j\psi(\xi)}$, obtained after extracting a proper phase function $\psi(\xi(s))$ and introducing a suitable parameterization $\xi(s)$ along the observation curve. A proper choice of these parameters leads to approximate the reduced field by a cardinal series of the kind:

$$F(\xi) = \sum_{n=1}^{N'} E\left(\xi_n\right) \cdot e^{-j\psi(\xi_n)} \Phi\left[w(\xi - \xi_n)\right] \tag{33}$$

where $\Phi(x)$ is the $\frac{sin(x)}{x}$ function or the Dirichlet function, $\xi_n = \frac{n\pi}{\chi \cdot W}$ are the positions of non-redundant sampling points, while N' represents the number of non redundant samples falling in the measurement interval.

The above relation, discretized in the M measurement points, say ξ_m, $m = 1, \ldots, M$, can be written in matrix form as (Costanzo et al., 2005):

$$\underline{r} = \underline{\underline{A}} \cdot \underline{s} \tag{34}$$

where $\underline{s}$ is the array of the reduced field values in the non redundant sampling positions and $\underline{r}$ is the corresponding array of the reduced field values at the measuring points . Due to the representation error and the presence of noise usually corrupting measurements, data do not

belong in general to the range of matrix $\underline{\underline{A}}$. Consequently, the following generalized solution is adopted:

$$\inf_{\Delta\phi_1,\ \Delta\phi_2,\ldots,\Delta\phi_{i-1}} d\left(S_m, S_A^N\right) \tag{35}$$

The term $d(.,.)$ into equation (35) represents the distance between the two sets, while S_A^N is the set of all reduced field (evaluated at the M measurement points) that the AUT can radiate.
The distance d between the two sets is numerically evaluated by introducing the projector operator $\underline{\underline{P}} = \underline{\underline{A}}\ \underline{\underline{A}}^+$ onto the range of matrix $\underline{\underline{A}}$, $\underline{\underline{A}}^+$ denoting the pseudoinverse of $\underline{\underline{A}}$. Consequently, the near-field phase retrieval involves the finding of:

$$\min_{\Delta\phi_1,\ \Delta\phi_2,\ldots,\Delta\phi_{i-1}} \left\| \underline{r}(\Delta\phi_1,\ \Delta\phi_2,\ldots,\Delta\phi_{i-1}) - \underline{\underline{P}}\ \underline{r}(\Delta\phi_1,\ \Delta\phi_2,\ldots,\Delta\phi_{i-1}) \right\|^2 \tag{36}$$

which can be easily performed by a suitable least-square procedure.

3.2 Experimental validations of hybrid phase-retrieval technique

The hybrid phase-retrieval technique is experimentally validated by designing a multifrequency prototype properly working within X-band. Two rectangular waveguides used as probes are connected to the microstrip circuit in Fig. 15(a) for obtaining the required amplitude information. Measurements are performed on a standard X-band pyramidal horn (Fig. 15(b)) by assuming a cylindrical scanning geometry of $47x85$ points along z and ϕ, respectively, with sampling steps $\Delta z = \lambda/2 = 1.5cm$ and $\Delta\phi = 4.23^o$ at different frequencies.

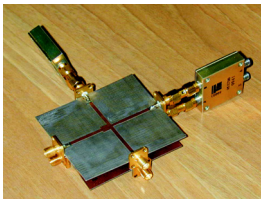

(a)

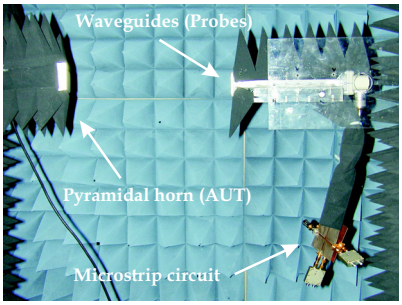

(b)

Fig. 15. (a) Microstrip circuit and (b) test setup for phaseless near-field measurements.

The near-field directly measured at one output of the integrated probe is reported under Figs. 16-17 for both amplitude and phase at two different frequencies, namely $f = 8GHz$ and $f = 10GHz$. The interferometric formula (29) is used in conjunction with the minimization procedure (36) to obtain the retrieved near-field phase, whose agreement with the exact one is illustrated under Figs. 16(b)-17(b) along the cylinder generatrix at $\phi = 90^o$.
The standard NF-FF cylindrical transformation (Leach and Paris, 1973) is then applied to obtain the far-field patterns of Figs. 18-19. In particular, a good agreement between results obtained from direct and retrieved near-field phase can be observed under Figs. 18(b)-19(b) for the H-plane.

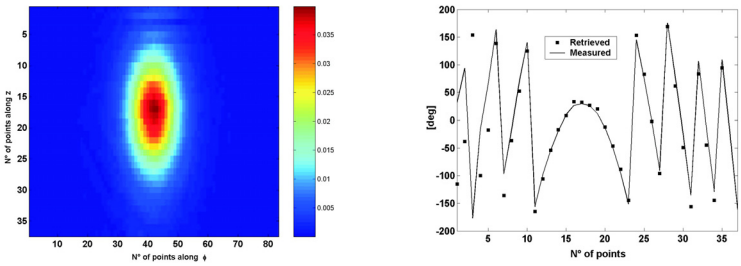

(a) (b)

Fig. 16. (a) Measured near-field amplitude on the cylindrical surface and (b) near-field phase (retrieved and measured) on the cylinder generatrix at $\phi = 90^o$: frequency $f = 8GHz$.

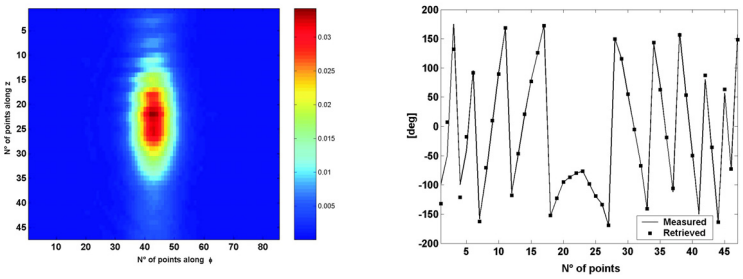

(a) (b)

Fig. 17. (a) Measured near-field amplitude on the cylindrical surface and (b) near-field phase (retrieved and measured) on the cylinder generatrix at $\phi = 90^o$: frequency $f = 10GHz$.

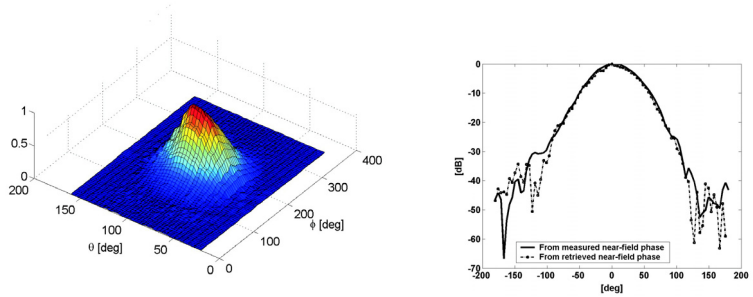

(a) (b)

Fig. 18. (a) 3-d view of radiation pattern and (b) H-plane obtained from exact and retrieved near-field phase: frequency $f = 8GHz$.

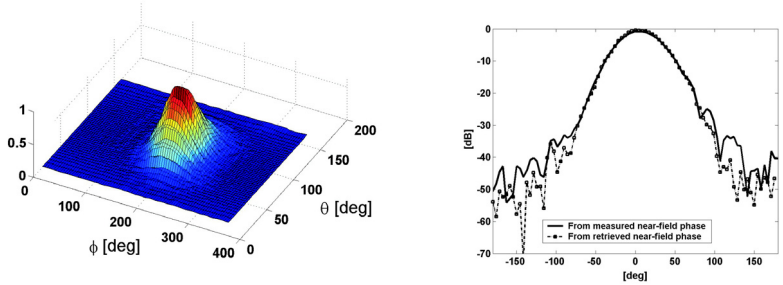

(a) (b)

Fig. 19. (a) 3-d view of radiation pattern and (b) H-plane obtained from exact and retrieved near-field phase: frequency $f = 10GHz$.

4. Conclusion

Innovative techniques for near-field antenna testing have been presented in this chapter. Two primary aspects, namely the reduction of both measurement time and cost setup on one hand, and the accurate near-field phase characterization on the other hand, have been accurately faced. For what concerns the first focus point, accurate and fast near-field to far-field transformations on new strategic geometries of helicoidal, plane-polar, bi-polar and planar spiral type have been presented. On the other hand, the problem of accurate phase retrieval at high operating frequencies has been faced by presenting a hybrid interferometric/functional-kind approach to obtain the antenna far-field pattern from a reduced set of amplitude-only near-field data acquired on a single scanning surface. All discussed procedures have been successfully validated by numerical and experimental tests.

5. References

Abramowitz, M. & Stegun, I. A. (1972). *Handbook of mathematical functions*,Dover, New York.

Bennet, J. C., Anderson, A. P., Mcinnes, P. A. & Whitaker, J. T. (1976). Microwave holographic metrology of large reflector antennas. *IEEE Trans. Antennas Propag.*, Vol. 24, (1976) page numbers (295-303).

Bracewell, R. N. (2000). *The Fourier Transform and Its Applications*, McGraw-Hill, ISBN 0-07-303938-1, Singapore.

Bucci, O. M., Gennarelli, C. & Savarese, C. (1998). Representation of electromagnetic fields over arbitrary surfaces by a finite and nonredundant number of samples. *IEEE Trans. Antennas Propag.*, Vol. 46, (1998) page numbers (351-359).

Costanzo, S., Di Massa, G. & Migliore, M. D. (2001). Integrated microstrip probe for phaseless near-field measurements on plane-polar geometry. *Electronics Letters*, Vol. 37, (2001) page numbers (1018-1020).

Costanzo, S. & Di Massa, G. (2002). An integrated probe for phaseless near-field measurements. *Measurement*, Vol. 31, (2002) page numbers (123-129).

Costanzo, S., Di Massa, G. & Migliore, M. D. (2005). Integrated microstrip probe for phaseless near-field measurements on plane-polar geometry. *IEEE Trans. Antennas Propag.*, Vol. 53, (2005) page numbers (1866-1874).

Costanzo, S. & Di Massa G. (2004). Far-field reconstruction from phaseless near-field data on a cylindrical helix. *Journal of Electromagn. Waves Applicat.*, Vol. 18, (2004) page numbers (1057-1071).

Costanzo, S. & Di Massa G. (2006). Efficient near-field to far-field transformation from plane-polar samples. *Microwave Opt. Tech. Letters*, Vol. 48, (2006) page numbers (2433-2436).

Costanzo, S. & Di Massa G. (2006). Direct far-field computation from bi-polar near-field samples. *Journal of Electromagn. Waves Applicat.*, Vol. 20, (2006) page numbers (1137-1148).

Costanzo, S. & Di Massa G. (2007). Near-field to far-field transformation with planar spiral scanning. *Progress In Electromagnetics Research, PIER*, Vol. 73, (2007) page numbers (49-59).

Costanzo, S. & Di Massa, G. (2008). Wideband phase retrieval technique from amplitude-only near-field data. *Radioengineering*, Vol. 17, (2008) page numbers (8-12).

Elliott, R. S. (2003). *Antenna theory and design*, IEEE Press, ISBN 0-471-44996-2, New York.

Isernia, T., Pierri, R. & Leone, G. (1991). New technique for estimation of farfield from near-zone phaseless data. *Electronics Letters*, Vol. 27, (1991) page numbers (652-654).

Isernia, T., Leone, G. & Pierri, R. (1996). Radiation pattern evaluation from near-field intensities on planes. *IEEE Trans. Antennas Propag.*, Vol. 44, (1996) page numbers (701-710).

Johnson, R. C., Ecker, H. A. & Hollis, J. S. (1973). Determination of far-field antenna patterns from near-field measurements . *Proc. of IEEE*, Vol. 61, (1973) page numbers (1668-1694).

Leach, M. W. & Paris, D. T. (1973). Probe compensated near-field measurements on a cylinder. *IEEE Trans. Antennas Propag.*, Vol. 21, (1973) page numbers (435-445).

Ludwig, A. C. (1971). Near-field far-field transformations using spherical-wave expansions. *IEEE Trans. Antennas Propag.*, Vol. 19, (1971) page numbers (214-220).

Pierri, R., D'Elia, G. & Soldovieri, F. (1999). A two probes scanning phaseless near-field far-field transformation technique. *IEEE Trans. Antennas Propag.*, Vol. 47, (1999) page numbers (792-802).

Wang, J. J. H. (1988). An examination of theory and practices of planar near-field measurements. *IEEE Trans. Antennas Propag.*, Vol. 36, (1988) page numbers (746-753).

Yaghajian, A. D. (1986). An overview of near-field antenna measurements. *IEEE Trans. Antennas Propag.*, Vol. 34, (1986) page numbers (30-45).